



Contribution of amorphous soft segments orientation and their strain induced crystallization to the elastocaloric effect of thermoplastic polyurethaneurea elastomers

Nicolas Candau ^{a,b,*}, Oguzhan Oguz ^c, Gizem Kurtulmus ^d, Emel Yilgor ^e, Yusuf Z. Menceloglu ^d, Iskender Yilgor ^e

^a eb-POLICOM - e-PLASCOM, Departament de Ciència i Enginyeria de Materials, Barcelona-Tech, Campus Diagonal Besòs-EEBE, Universitat Politècnica de Catalunya, Barcelona, 08019, Spain

^b Center for Research in Multiscale Science and Engineering of Barcelona, Barcelona-Tech, Campus Diagonal Besòs-EEBE, Universitat Politècnica de Catalunya, Barcelona, 08019, Spain

^c Mettler-Toledo GmbH, Analytical, 8606, Nänikon, Switzerland

^d Faculty of Engineering and Natural Sciences, Materials Science and Nano Engineering, Sabanci University, Orhanli, Tuzla, Istanbul, 34956, Turkey

^e KUYTAM Surface Science and Technology Center, Chemistry Department, Koc University, Sarıyer, Istanbul, 34450, Turkey

ABSTRACT

This study investigates the mechanisms underlying the elastocaloric (eC) effect in thermoplastic polyurethaneurea elastomers, focusing on the contributions of amorphous chain orientation and strain-induced crystallization (SIC) of the soft segments. Two types of TPU systems—strain induced crystallizable (PTMO-based polyurethaneurea (TPUU)) and non-crystallizable (PEO-based polyurea (TPU))—were synthesized with different amounts of HMDI hard segments (20 or 30 wt%) and subjected to mechanical loading under *in situ* wide-angle X-ray scattering (WAXS) and infrared thermography. The amorphous chain orientation is found to evolve much faster with strain in the TPUUs and SIC is found to initiate in these materials above a critical value of the Hermann's orientation factor of 0.7–0.75. SIC in these systems is found to enhance the eC effect via latent heat, but amorphous orientation is also found to significantly contribute through thermoelastic entropy changes, as attested by high heat sources of 15 MW m^{-3} for crystallizable TPUU before SIC (at 100 % of deformation) as compared to 5 MW m^{-3} for non-crystallizable TPUs. Under continuous cycles, TPUU samples demonstrate stronger eC responses and greater reversibility than TPU, resulting in higher coefficients of performance (Best COP = 13 for the TPUU20), particularly after cyclic pre-conditioning. This interpretation of molecular orientation and crystallization in relation with eC properties opens new design strategies for polymer-based solid-state cooling, where microstructural tailoring—beyond relying solely on crystallization—can optimize elastocaloric performance in practical applications.

1. Introduction

The elastocaloric effect (eC) is a solid-state cooling mechanism based on the reversible temperature change that occurs when a material is mechanically deformed and relaxed under adiabatic conditions [1,2]. Compared to vapor-compression technologies, eC-based systems promise greater energy efficiency, environmental sustainability, and mechanical simplicity [3]. Among soft materials, elastomers stand out due to their low modulus, high strain capability, and potential for recyclability, making them attractive candidates for scalable, flexible, and lightweight cooling systems [4–8].

Initial studies have focused on materials such as natural rubber (NR) [7,9,10], highlighting their ability to undergo significant elastic

deformation and exhibit reversible temperature changes upon cyclic loading. The caloric effect in natural rubber is thought to be due to its high ability to crystallize under strain as compared to other synthetic rubbers. A tentative quantification concluded that 1/3 of the elastocaloric effect was attributed to thermoelasticity and 2/3 to the strain induced crystallization [7] under uniaxial stretching. The crystallization being reversible, during unloading, the same 2/3 proportion to the overall cooling of the material has been attributed to the melting of the strain induced crystalline phase. In spite of these efficient entropy-driven mechanisms for heating and cooling, NR may suffer from processing limitations and variable fatigue performance, motivating the search for synthetic alternatives with tunable properties and better control over composition and microstructure.

* Corresponding author. eb-POLICOM - e-PLASCOM, Departament de Ciència i Enginyeria de Materials, Barcelona-Tech, Campus Diagonal Besòs-EEBE, Universitat Politècnica de Catalunya, Barcelona, 08019, Spain.

E-mail address: nicolas.candau@upc.edu (N. Candau).

Thermoplastic polyurethanes (TPUs) have emerged as promising elastocaloric materials [11–14]. Traditionally used in flexible foams, rigid insulations, and coatings, TPUs exhibit high processability [15–17], high thermal and mechanical performance [18–22], high durability [23,24] and chemical resistance [25–27] making them promising candidates for eC applications. When carefully synthesized, polyurethanes can approach the outstanding mechanical toughness of natural rubber [28], while also offering recyclability, self-healing, and enhanced thermal stability [29]. Like NR, the ability of TPUs to undergo strain-induced crystallization has been widely demonstrated in the literature [30–33]. This crystallization is driven by microphase separation, hard segment symmetry, and chain alignment under stress. SIC is promoted in TPU by microphase separation that refers to the spontaneous segregation of the polymer into distinct hard and soft domains at the nanometer scale, typically with domain size in the range of 10–100 nm, that act as physical cross-links. The hard Segment Domains act as reinforcing regions, increasing stiffness and strength. The Soft Segment Domains maintain flexibility and allow for large deformations. In some TPUs, SIC results in an additional mechanical reinforcement.

Both PTMO-based and PEO-based polyurethanes are known to exhibit strain-induced crystallization (SIC) due to the ability of the PTMO [16,17,30,33] and PEO [34–37] soft segments (SS) to align and order under tensile deformation, which is promoted by microphase separation. Wide-angle X-ray scattering (WAXS) confirmed the formation of strain-induced crystalline structures in PTMO-based and PEO-based polyurethanes.

SIC of the soft segment in TPUs has been argued to be a primary cause of the eC effect in these materials, especially in formulations based on crystallizable blocks like poly(tetramethylene oxide) (PTMO). Other studies interestingly show that elastocaloric effects can also be generated in absence of significant crystallization [38]. Under mechanical deformation, polymer chains in the amorphous phase align along the loading axis, reducing configurational entropy and thus generate a thermal response (thermoelasticity) even in the absence of crystallization.

In this study, we provide direct microstructural evidence that both SIC and amorphous SS chain orientation contribute to the elastocaloric effect in TPU-based systems. For the first time, a combination of *in situ* wide-angle X-ray scattering (WAXS) and infrared thermography, is used to examine TPUUs and TPUs with crystallizable (PTMO-based) and non-crystallizable (PEO-based) soft segments respectively, in the strain range studied. We analyze the evolution of crystallinity, chain orientation (via Herman's orientation factor), and temperature change during cyclic loading at various strain levels and pre-strains. Our findings support a mechanism interpretation where amorphous SS orientation plays a significant role in the early stages of deformation and remains relevant in systems with weak or no SIC. Nonetheless, occurrence of SIC is thought to provide a non-negligible source of supplementary eC effect through latent heat of phase change in both crystallization and melting processes. These insights open the door to new material design strategies where eC efficiency is enhanced through tailored microstructure control rather than relying solely on crystallization processes.

2. Materials and experiments

2.1. Materials

Bis(4-isocyanatocyclohexyl)methane (HMDI) was kindly supplied by Bayer and had a purity better than 99.5 %. Poly(tetramethylene oxide) glycol (PTMO2K) with $\langle M_n \rangle = 2040$ g/mol was provided by DuPont. Amine terminated poly(ethylene oxide) oligomer (PEO2K) with $\langle M_n \rangle = 2070$ g/mol (Jeffamine ED2000) was supplied by Huntsman Corporation. Reagent grade ethylene diamine (ED), 2-propanol (IPA) and tetrahydrofuran (THF) were purchased from Merck. Dibutyltin dilaurate (DBTDL) was obtained from Witco and is used as a catalyst by diluting to 1 % by weight in THF. All chemicals were used as received.

2.2. Polymer synthesis

All reactions were carried out in 500 mL, three-necked round-bottom Pyrex reaction flasks, equipped with a mechanical overhead stirrer, a thermometer, and a dropping funnel. Reaction temperature was adjusted using an electric heating mantle. All polymers were synthesized in solution by using the two-step polymerization procedure, as described below. Polymer solutions obtained were cast into Teflon molds and the solvents were evaporated by keeping at room temperature for overnight and then in a vacuum oven at 60 °C until constant weight. Compositions of the polymers synthesized are provided in Table 1.

2.3. Synthesis of PTMO2K based polyurethaneureas (TPUU)

Depending on the hard segment content of the final polyurethaneurea, calculated amounts of HMDI and PTMO2K were weighed into the reactor and dissolved in THF to prepare a solution with solids content of about 40 % by weight. 150 ppm of DBTDL was added into the solution and the system was heated to 60 °C, under 150 rpm stirring rate. Prepolymer formation reaction, followed by Fourier transform infrared (FTIR) spectroscopy, was completed in about 2 h. Reaction mixture was cooled down to room temperature and diluted to 30 % solids by IPA addition. Stoichiometric amount of ED chain extender was dissolved in IPA (10 % by weight solids), introduced into the dropping funnel and added dropwise onto prepolymer solution at room temperature under 250 rpm stirring rate. ED addition was stopped when the isocyanate peak centered at 2260 cm⁻¹ completely disappeared, indicating the completion of the reaction.

2.4. Synthesis of PEO2K based polyureas (TPU)

Depending on the hard segment content, calculated amount of HMDI was introduced into the reactor and dissolved in IPA to make a 20 % by weight solution. Separately PEO2K was dissolved in IPA (20 % solution), introduced into the dropping funnel, and added dropwise into HMDI solution at room temperature under 150 rpm stirring rate. Stoichiometric amount of ED chain extender was dissolved in IPA (10 % by weight solids), transferred into the dropping funnel and added dropwise into prepolymer solution at room temperature under 250 rpm stirring rate. ED addition was stopped when the isocyanate peak centered at 2260 cm⁻¹ completely disappeared, indicating the completion of the reaction. As the viscosity increased upon chain extension, reaction mixture was diluted with IPA to desired viscosity. Molecular weight, molecular structure of PTMO-2000 based polyurethaneureas (TPUU) and PEO-2000 based polyurea (TPU)s are shown in Table 1, Supplementary Fig. S1 and the hard segment contents (wt.%) and average chain lengths of the hard segments in TPUU and TPU copolymers investigated is shown in Supplementary Fig. S2.

2.5. Fourier-transform infrared (FTIR) spectroscopy and gel permeation chromatography (GPC)

FTIR spectra were obtained on a ThermoScientific Nicolet 6700 spectrometer. Thin films were coated on KBr discs, solvent was evaporated using a heat gun and the spectra were obtained with a resolution of

Table 1

Compositions, average molecular weights, and molecular weight distributions (PDI) of TPUU and TPU polymers.

Polymer code	Soft segment type	Hard segment content (wt%)	$\langle M_n \rangle$ (g/mol)	$\langle M_w \rangle$ (g/mol)	PDI
TPUU-20	PTMO2K	22.2	38,000	112,000	2.95
TPUU-30	PTMO2K	30.6	25,000	56,000	2.24
TPU-20	PEO2K	22.8	33,000	88,000	2.67
TPU-30	PEO2K	30.3	—	—	—

4 cm⁻¹. GPC analysis was carried out on a Viscotek GPCmax VE-2001 instrument equipped with D5000-D 3000-D 1000-D Guard columns and refractive index (RI), multiple angle laser light scattering (MALLS) and viscometer (TDA 305) detectors. DMF was used as the solvent and measurements were made at 55 °C, at a flow rate of 0.7 mL/min. Polymer solution was prepared in DMF at a concentration of 2 mg/mL. The samples were filtered using VMR PTFE syringe filters with average pore size of 0.22 µm prior to the measurements. Calibration curves based on poly(methyl methacrylate) standards were used. Densities of the films were determined using mass-volume relationship.

2.6. In-situ wide angle X-rays scattering (in-situ WAXS)

We performed in situ WAXS experiments at synchrotron ALBA in Cerdanyola del Vallès (Barcelona), using the beamline BL11-NCD-SWEET of ALBA synchrotron. The beam has a wavelength of 0.957 Å and the time of exposure of the sample is of 1 s. The latency time, needed for the acquisition of the diffraction image is 5.1 s. A single hybrid-pixel photon counting detector, model LX255-HS (Rayonix), with an active area of 85 × 255 mm², composed of 1920 x 5760 pixels with a pixel size of 88.54 × 88.54 µm², is positioned perpendicularly to the beam for the acquisition of the images. The distance between the detector and the sample is of 229.860 mm. The sample positioning system used, is the Stretcher - TST3508, which is capable of temperature and force control, with a force resolution of 0.01 N and a maximum stretching amplitude of 45 mm. The background, (i.e. air scattering and direct beam intensities) is properly measured in absence of any sample. It can then be subtracted to the total intensity scattered in the presence of the rubber sample. Each scattering pattern is integrated azimuthally. The deconvolution of the curve $I = f(2\theta)$ enables the extraction of the intensity at the peak top and the width at half height of each crystalline peak and the intensity at the peak top of the amorphous phase. The crystallinity index CI is calculated as a function of the intensity of the (100) and (010) crystallographic planes and of the amorphous halo, I_a , and expressed as:

$$CI(\%) = \frac{I_{100} + I_{010}}{I_{100} + I_{010} + I_a} \quad (1)$$

Textures of the crystallographic and amorphous structures can be characterized using the Herman's orientation function [39,40]:

$$\langle P_2 \rangle_a = \frac{1}{2} (3(\cos^2 \varphi) - 1) \quad (2)$$

$\langle P_2 \rangle_a = 1$ for perfect alignment of the amorphous chains with the tensile axis, $\langle P_2 \rangle_a = 0$ for random orientation, and $\langle P_2 \rangle_a = -0.5$ if the amorphous chains are preferentially oriented in the plane perpendicular to the tensile axis. $\langle P_2 \rangle_a$ may be obtained from the variation in intensity with azimuthal scattering angle, φ , of the corresponding Debye ring in a two-dimensional WAXS pattern with the X-ray beam perpendicular to the tensile axis, using:

$$\langle P_2 \rangle_a = \frac{1}{2} \left(3 \frac{\int_0^{\pi/2} I_a(\varphi) \cos^2 \varphi \sin \varphi d\varphi}{\int_0^{\pi/2} I_a(\varphi) \sin \varphi d\varphi} - 1 \right) \quad (3)$$

2.7. Differential Scanning calorimetry (DSC)

DSC thermograms were obtained on a DSC Q2000 series instrument (TA Instruments, New Castle, DE, USA). Approximately 10–11 mg of material was sealed in a standard 40 µL aluminum pan. The samples were equilibrated at -50 °C for 5 min and then heated to 100 °C at a rate of 5 °C/min under nitrogen atmosphere with a modulation amplitude of ±0.318 °C and a modulation period of 60 s. Samples were then cooled down to -50 °C and heated again up to 100 °C. Temperature and enthalpy calibrations of DSC was obtained by using antimony and tin standards.

2.8. Tensile tests with in-situ Infra-red thermography (in-situ IR)

Room temperature uniaxial tensile tests were performed on a universal testing machine ZwickRoell (Z005) equipped with a 500 N force sensor. The crosshead speed during the loading and unloading phases was chosen to be 3000 mm/min corresponding to a nominal strain rate of around 1×10^2 min⁻¹ according to the specimen dimensions (28 mm length). In the first type of tensile tests, the rubber specimens were stretched during single uniaxial stretching up to failure. In the second type of tensile tests, the rubber specimens were rapidly stretched with the nominal strain rate of 1×10^2 min⁻¹ up to 300 % elongation followed by a relaxation step in the deformed state for 1 s or 1 min. After the relaxation step, the specimens were unloaded with the same nominal strain rate of 2×10^2 min⁻¹ down to the relaxed state (zero force) followed by another relaxation for one more minute. The temperature field on the front face of the samples was recorded using an Infrared (IR) camera (InfraTech ImageIR® 8800) equipped with a Mercury–Cadmium–Telluride (MCT) detector with a temperature resolution at 30 °C higher than 0.035 K. The distance between the IR camera and the specimen was chosen sufficiently large to ensure that the sample surfaces can be observed from the undeformed state to the deformed state, but sufficiently low to record images with sufficiently fine pixel size (200 µm). The size of the observation zone is 160 × 500 pixels² (32 × 100 mm²). Image data was synchronized with analogical data of the tensile test machine, namely time, force, and displacement between the grips. The acquisition frequency of the IR images was chosen to be equal to 100 Hz to capture fast temperature changes that may occur within the different phases of the tests. The IRBIS 3.1 professional software (InfraTech ImageIR® 8800) was used to extract punctual temperature values along the specimen longitudinal axis. The central part of the specimen where the temperature data was extracted shows a homogeneous temperature field at the mm scale.

2.9. Analysis of the heat sources

The calculation of heat source and sink is of prime importance to fully describe the eC phenomena in NR and NR/GTR and discriminate the diverse contribution of thermoelasticity, strain induced crystallization, melting, viscoelasticity and damage involved in the materials heating and cooling performances. Thermoelasticity and crystallization/ melting are elastic reversible processes, while damage and viscoelasticity are inelastic processes. To estimate heat sources/sink, only the temperature at the specimen surface in the central part of the tensile bars is considered where the temperature field is spatially homogeneous. Hence, the heat source distribution is uniform within the considered area of interest. A linearization of heat losses in the heat equation results in the following expression of the heat source [41,42]:

$$S = \rho C_p \left(\dot{\theta} + \frac{\theta}{\tau} \right) \quad (4)$$

S is the heat source expressed in MW.m⁻³, $\rho = 1.1$ g cm⁻³ is the bulk density of the tested material, C_p its heat capacity is around 1.6 J g⁻¹K⁻¹ for all materials at room temperature and is assumed to not significantly change with possible changes of the specimen surface during tensile tests, $\theta = T - T_0$, the temperature variation above (positive) or below (negative) the equilibrium room temperature, T_0 . $\dot{\theta}$ is the rate of heating (K.s⁻¹). The time constant τ (s) characteristic of the heat exchange (during heating or cooling) along the specimen thickness was calculated using the following equation:

$$\theta = (T_{t=0} - T_0) e^{-\frac{t}{\tau}} \quad (5)$$

With $T_{t=0}$ and T_0 being the temperatures at the beginning and at the end of the relaxation step respectively, after the specimen has been heated (during loading) or cooled (during unloading). The thermal relaxation times is expected to decrease with the applied deformation, that is

explained by the reduction of the specimen thickness when applying a longitudinal strain. Indeed, if we assume a volume conservation in our materials subjected to loading, the materials thickness would be equal $e_0/\sqrt{\lambda}$ with e_0 being the thickness of the material in the undeformed state and λ the stretching ratio, equal to $1+\epsilon$, ϵ being the strain. The dependence of the thermal diffusion time on the applied deformation can be evaluated assuming that this time decreases similarly with the thickness reduction upon tensile deformation:

$$\tau = \tau_0 / \sqrt{\lambda} \quad (6)$$

The relationship between mechanical dissipation and thermal dissipation during cyclic loading is provided by the calculation of the corresponding dissipated energies. The mechanical energy W_{def} is split into elastic W_e and inelastic W_{in} parts. The former part is the recoverable elastic energy per unit of volume. The latter part, i.e., the total inelastic energy per unit volume, is made of intrinsic dissipation ϕ_1 and stored energy per unit volume W_s . In the following, the elastic component per cycle remains close to zero and it can be considered that the mechanical and inelastic energy per unit volume per cycle are approximately the same. The deformation energy is then written:

$$W_{def} = \phi_1 + W_s \quad (7)$$

The hysteresis loops that characterize the deformation energy loss is essentially due to material dissipation. In the absence of microstructural transformations, the area of the surface of the hysteresis loop is equal to the amount of energy dissipated in the material over a complete loading cycle. The mechanical energy per cycle was estimated using the expression below

$$W_{def} = \int \frac{Fde}{e_0 L_0} \quad (8)$$

The mean dissipation energy rate over a cycle $\sim \phi_1$ was then calculated via the zero-dimensional approach of the local heat diffusion equation:

$$\phi_1 = \rho C_p \int \left(\dot{\theta} + \frac{\theta}{\tau} \right) dt \quad (9)$$

The materials coefficient of performance, COP_{mat} , measured during a cyclic loading, is given by the following formula:

$$COP_{mat} = \frac{\phi_1}{W_{def}} \quad (10)$$

3. Results and discussion

3.1. Thermal crystallization in TPU and TPUU

We investigate the thermal crystallization of two sets of materials: TPUU and TPU (in the strain range studied) that is attributed to the higher ability of amorphous PTMO soft segment chains in TPUU to orient as incipient mechanism for SIC. As a preliminary characterization before the investigation of the eC effect, we aimed at providing data on thermal stability of the crystalline phase at room temperature and above. The aim is to understand the possible changes in the microstructure eventually induced by the self-heating of the materials during mechanical loading. For this purpose, we performed DSC experiments, where we first heated the specimens up to 100 °C, and then cooled them down to -50 °C where they were equilibrated for 5 min, which was followed by a second heating up to 100 °C. It is found that in amorphous materials (obtained after first heating up to 100 °C), when cooled down, result in the crystallization. The crystallization temperature for TPU20 and TPUU20 is found equal to 2–4 °C, whereas TPU30 crystallizes at -43 °C and TPUU30 does not crystallize in the cooling temperature range (Fig. 1a). Results indicate a higher ability of the PEO-based TPU to thermally crystallize as compared to the PTMO-based TPUU. In

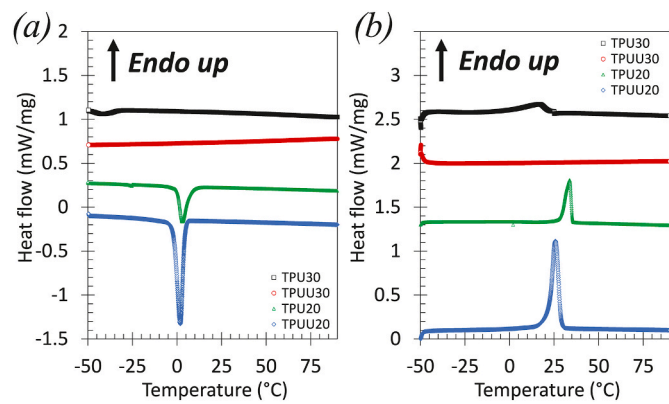


Fig. 1. DSC experiments performed on PUs. (a) Heat flow versus temperature curves for cooling from 100 °C down to -50 °C and (b) Heat flow versus temperature curves for heating from -50 °C up to 100 °C.

addition, TPU20 and TPUU20 crystallize easily as compared to TPU30 and TPUU30. In an analogy with vulcanized natural rubber, a higher quantity of hard segments (that would play the same restrictive role that the intermolecular chemical crosslinks in vulcanized NR) may hinder molecular diffusion and hence hinder thermal crystallization. This does not happen for SIC (previously described results) as SIC and in particular the nucleation is mostly promoted by forced molecular orientation (of both hard and soft segments). Melting of the crystalline phase occurs at 25 °C and 33 °C for TPUU20 and TPU20 respectively, and at 17 °C for TPU30, while amorphous TPUU30 remains totally amorphous (Fig. 1b). To avoid traces of crystallinity in our materials, specimens were pre-heated at 40 °C before tensile tests (in-situ WAXS and in-situ IR).

3.2. Amorphous chains orientation and strain induced crystallization (SIC) in TPU and TPUU

The contributions of the orientation and crystallization of amorphous soft segment chains in TPU and TPUU are studied and their contribution to the elastocaloric effect in such materials may be of great importance. First, cyclic tensile tests performed on TPU and TPUU (Fig. 2) show distinct behavior depending on the content of the HMDI + ED hard segments (HS) (22 or 30 %) and on the chemical structure of the soft phase (PTMO or PEO). In the strain range studied, all materials show a viscoelastic behavior typical for elastomeric materials. By extending up to 300 %, they show mechanical hysteresis that may be attributed primarily, and in absence of further microstructural observations, to viscoelastic effects (soft phase chains disentanglements, chains friction) or damage (chains breakage from the soft and hard phases). No evident

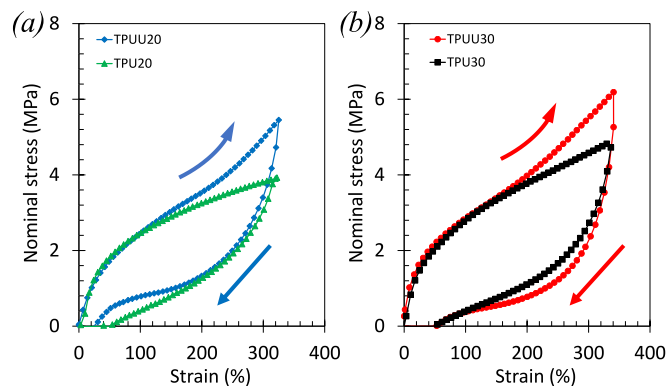


Fig. 2. (a) Stress-strain curves of TPUU20 (PTMO-2K with 22 % HMDI) and of TPU20 (PEO-2K with 22 % HMDI) and (b) Stress-strain curves of TPUU30 (PTMO-2K with 30 % HMDI) and of TPU30 (PEO-2K with 30 % HMDI).

sign of plastic mechanisms is observed (no yielding point or plastic plateau). A large strain reinforcement is observed in the strain range studied, in the case of TPUU as compared to TPU with similar hard segment contents. Such mechanical reinforcement in elastomeric thermoplastic polyurethanes may be attributed to their ability to crystallize under strain, as it has been widely demonstrated in the literature [37,43, 44].

To investigate the strain induced crystallization in both TPUU and TPU, in-situ WAXS have been performed (Fig. 3). In the undeformed state all materials are amorphous, as shown by the isotropic amorphous halo along azimuthal angle. Upon deformation, no apparent significant modification of this halo is observed for the PEO-based TPU systems. Contrarily, a clear anisotropy of the scattering pattern and in particular the formation of anisotropic crystalline features is observed in the case of the PTMO-based TPUU materials, where WAXS shows the meridional region peaks observed at Bragg angle values $2\theta = 12.2^\circ$ and $2\theta = 14.7^\circ$, corresponding to the d-spacings of (100) and (010) peaks for PTMO

crystal, which are reported to be around 4.5 \AA and 3.8 \AA , respectively [44]. Such observations reveal the occurrence of the strain induced crystallization in TPUU, that is found to be reversible, as shown by the disappearance of such crystalline features upon unloading. Consistent with the study of Yeh et al. [44], strain induced crystallization in PTMO based PU is found to be reversible. Such reversibility of SIC in PTMO based materials has also been discussed elsewhere [33,43]. While PEO-based TPUs do not show SIC in the strain range studied, we do not state that SIC cannot happen at higher deformations.

To assess the evolution of the crystalline fraction generated by the strain induced deformation, equation (2) has been used (Section 2.6). The crystalline fraction of TPUU20 and TPUU30 is shown in Fig. 4. Strain induced crystallization occurs in both materials at a deformation around 100 %, which regularly increases with strain. During unloading, the crystalline fraction decreases down to zero at a deformation of 50 %. The strain at crystallization onset is concomitant with the stress upturn observed on the stress-strain curves (see Fig. 2). SIC is hence expected to

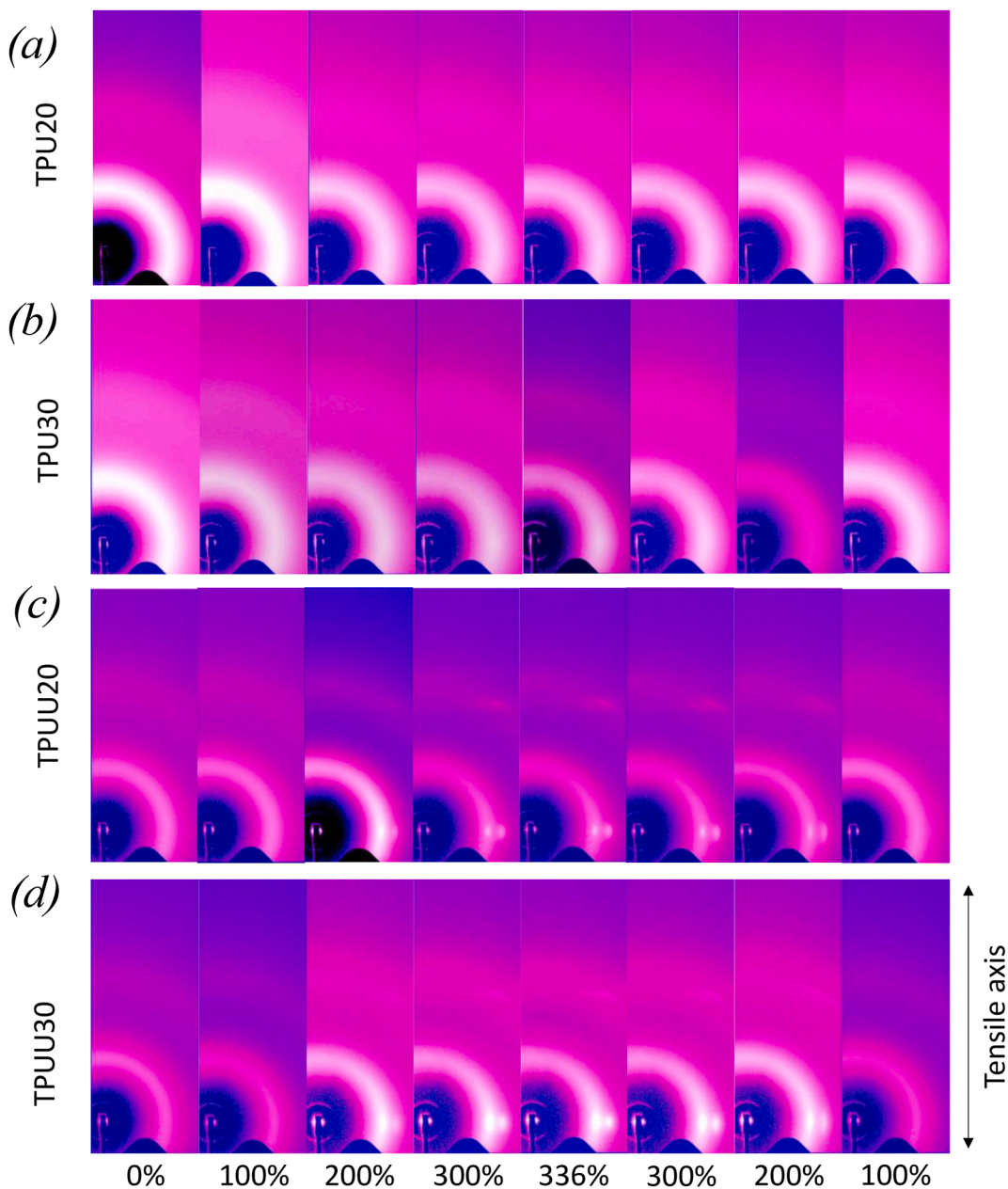


Fig. 3. (a) WAXS patterns of TPU20 (PEO-2K with 22 % HS), (b) TPUU20 (PTMO-2K with 22 % HS), (c) TPU30 (PEO-2K with 30 % HS), (d) TPUU30 (PTMO-2K with 30 % HS).

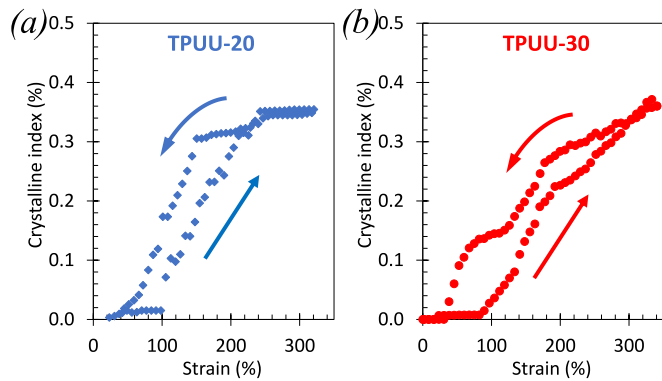


Fig. 4. (a) Crystalline fraction of TPUU20 (PTMO-2K with 22 % HS), (b) Crystalline fraction of TPUU30 (PTMO-2K with 30 % HS). The quantification of the crystallinity index is not realistic in the sense that it does not attest for the volumetric fraction for the strain induced crystal phase. Very high values of the CI may arise from.

be responsible of mechanical reinforcement, where PTMO SIC crystals play the role of temporary oriented nanofillers, equivalent to what may happen in vulcanized natural rubber [45]. One may note that, like for the natural rubber-based materials, a crystalline hysteresis is found, that

can be attributed to the distinct nature of crystallization and melting processes in a fully amorphous elastomer, in which crystallization requires the jumping of a nucleation barrier (high energy level, i.e., high deformation) while melting occurs in a semi-crystalline material with an existing interface between amorphous and crystalline phases (low energy level, i.e., low deformation). It is not obvious from the literature that PTMO-based TPUU has a higher ability to crystallize under strain as compared to PEO-based TPU, hence the molecular mechanisms prior the occurrence of SIC in PTMO based polyurethanes are investigated.

The probability of SIC to initiate (formation of the nuclei) is intrinsically related to the ability of the amorphous polymeric chains to align along a stretching axis, hence promoting molecular packing, at the origin of the crystallite formation. The quantity of amorphous chains aligned in the stretching axis as well as their orientation has been investigated (Fig. 5). Deformation of the TPU and TPUU results in a decreasing intensity of the amorphous signal in the equatorial region. One may note that such decrease may relate to the decrease of the specimen volume irradiated with strain due to thickness reduction. Nonetheless, such information remains relevant when comparing relatively the TPU and TPUU materials. It is worth noting that the decrease of intensity of the amorphous chains in the equatorial region is interrupted (it reaches a threshold) at a deformation of around 100 %, concomitant with the occurrence of SIC (cf. Fig. 4). The orientation of amorphous chains in the tensile axis, calculated using the Herman's orientation factor (Equations 2-3), is found to increase with strain for all

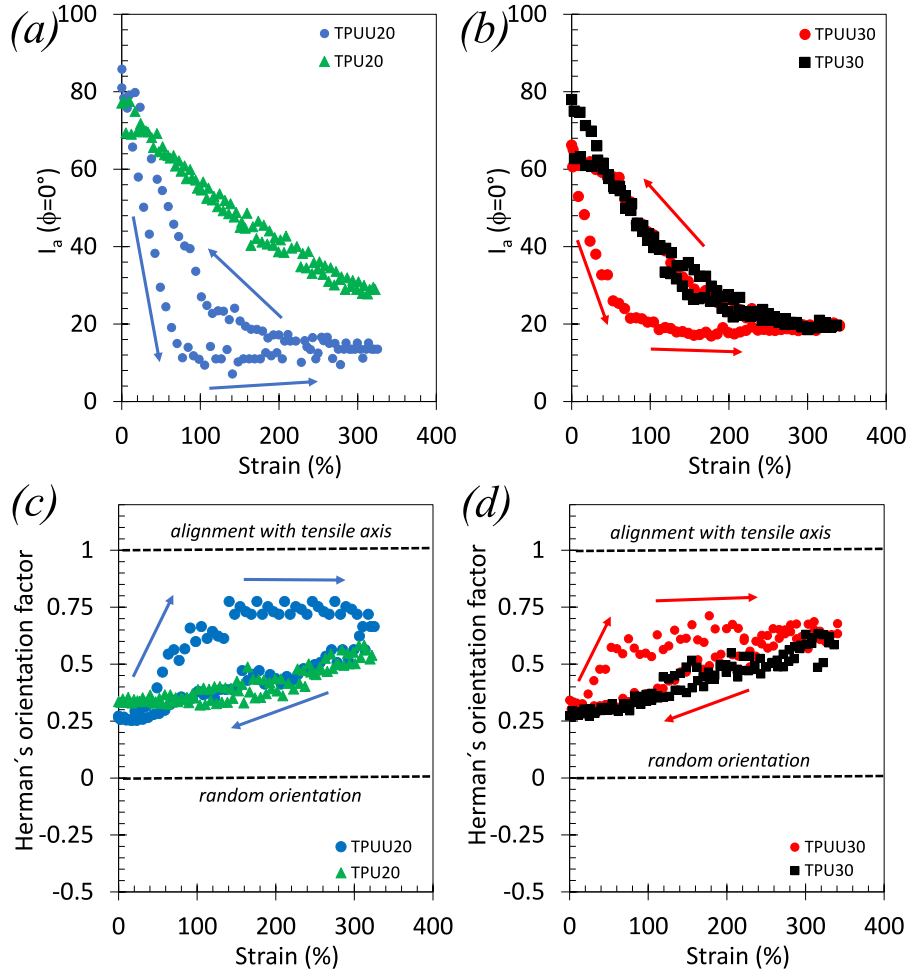


Fig. 5. (a) Intensity of the amorphous halo in the equatorial region of TPU20 (PEO-2K with 22 % HS) and TPUU20 (PTMO-2K with 22 % HS), (a) Intensity of the amorphous halo in the equatorial region of TPU30 (PEO-2K with 30 % HS) and TPUU30 (PTMO-2K with 30 % HS), (c) Herman's orientation factor (equations (2) and (3)) of the amorphous halo TPU20 (PEO-2K with 22 % HS) and TPUU20 (PTMO-2K with 22 % HS), (d) Herman's orientation factor (equations (2) and (3)) of TPU30 (PEO-2K with 30 % HS) and TPUU30 (PTMO-2K with 30 % HS).

materials, and then decrease during unloading (Fig. 5c–d). Interestingly, no hysteresis is observed in the case of non-crystallized TPU, and a hysteretic behavior is observed in the case of TPUU. Such hysteresis may be related to SIC occurrence: at a given deformation, the amorphous chains orientation in TPUU is higher during the loading phase, when the crystalline fraction is lower (see Fig. 4). This may be explained by the progressive disappearance of the amorphous signal that contributes to the crystal one. Highly oriented amorphous chains tend to crystallize and hence do not contribute in the calculation Herman's orientation factor. During loading, a critical value of the Herman's orientation factor of 0.75 is reached for the TPUU materials, that is assumed to be the critical value to initiate SIC. After such critical value, a plateau is observed and molecules that are oriented beyond such critical value are crystalline, and likely continue to orient (but in crystalline state). For TPU materials, such a value is not reached, suggesting that the orientation of amorphous chains is not sufficient to initiate SIC in the strain range studied. To conclude, rapid amorphous chains orientation in TPUU until a critical value is thought to be the incipient mechanism at the origin of strain induced crystallization of such materials. The difference in abilities to crystallize under strain of both types of PUs may find several origins. One possibility is related to the difference in the number of carbon atoms in PTMO ($\text{CH}_2\text{--CH}_2\text{--CH}_2\text{--CH}_2\text{--O}$) versus PEO ($\text{CH}_2\text{--CH}_2\text{--O}$). PTMO with 4 CH_2 units may pack better under strain than PEO, which has 2 CH_2 units linked together with flexible ether linkages. The important preliminary result related to the amorphous/crystalline deformation mechanisms in PUs is consistent with real-time mechano-optical studies, substantiated by offline characterization (AFM, SAXS, WAXS), that revealed the complex mechanisms of hard-soft segment deformation and concluded that there is a critical soft segment length beyond which strain-induced crystallization can occur [46,47].

3.3. Elastocaloric effect in TPU and TPUU

To study the elastocaloric effect in TPU and TPUU, single and cyclic tensile tests have been performed at high strain rate to work close to adiabatic conditions (Figs. 6–13). Fig. 6 illustrates the temperature field at specimen surface during loading and unloading (after return to equilibrium temperature) of a specimen of TPUU20 and TPUU30. Temperature increased more than 25°C above room temperature during loading and decreases down to $8\text{--}10^\circ\text{C}$ below room temperature during unloading. Temperature field in the central part of the specimen is found to be homogeneous in both loading and unloading phases, where maximum and minimum temperatures are recorded.

Nominal stress and temperature at specimen center during loading up to failure have been recorded (Fig. 7). Both stress and temperature rise are found to be higher in the full range of deformation for TPUU20

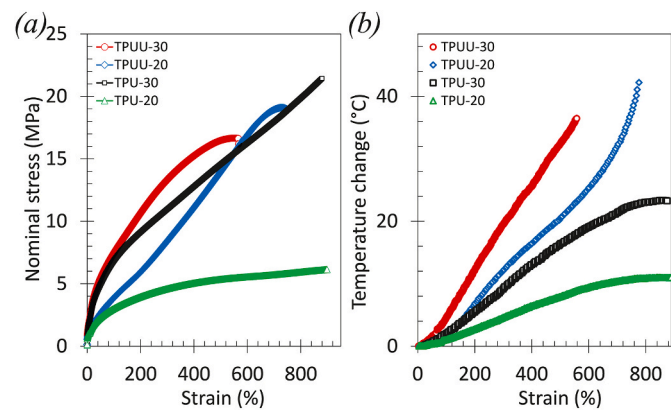


Fig. 7. (a) Nominal stress of TPU20 (PEO-2K with 22 % HS), TPUU20 (PTMO-2K with 22 % HS), TPU30 (PEO-2K with 30 % HS) and TPUU30 (PTMO-2K with 30 % HS) and (b) temperature at specimen surface of the same materials during single loading up to failure.

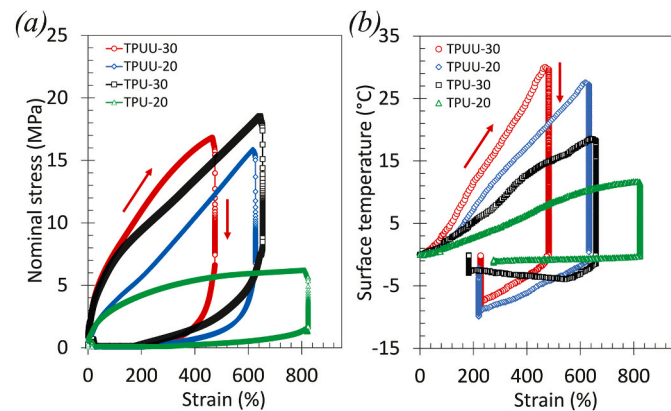


Fig. 8. (a) Nominal stress of TPU20 (PEO-2K with 22 % HS), TPUU20 (PTMO-2K with 22 % HS), TPU30 (PEO-2K with 30 % HS) and TPUU30 (PTMO-2K with 30 % HS) and (b) temperature at specimen surface of the same materials during a cyclic test consisting of loading, relaxation of 1 min, unloading and relaxation of 1 min.

as compared to TPU20 and for TPUU30 as compared to TPU30. Nonetheless, such difference in temperature rise is found to be predominant at large strain. This suggests that the elastocaloric effect likely results from the sum of several deformation mechanisms from low deformation up to

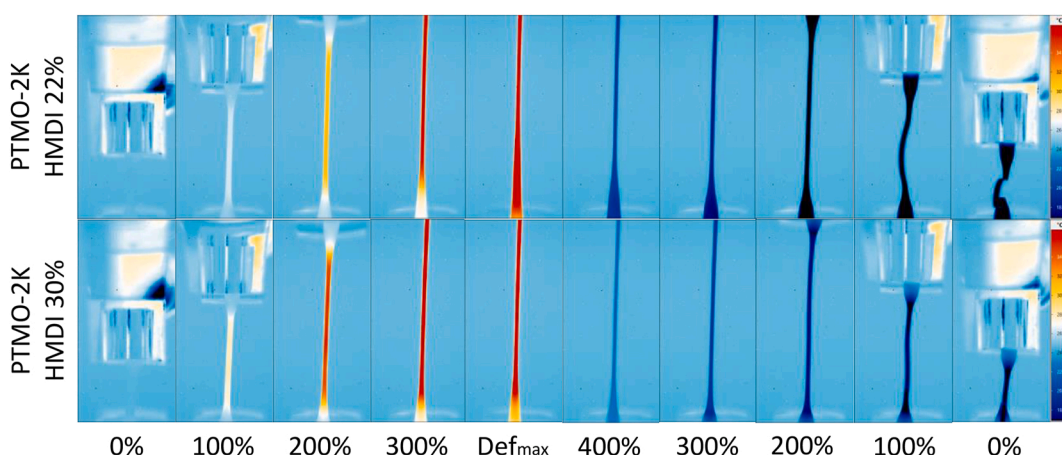


Fig. 6. Temperature field at specimen surface during loading and unloading, after a phase of relaxation of 1 min to allow return to ambient temperature between the two phases in case of TPUU30 (a) and TPUU20 (b).

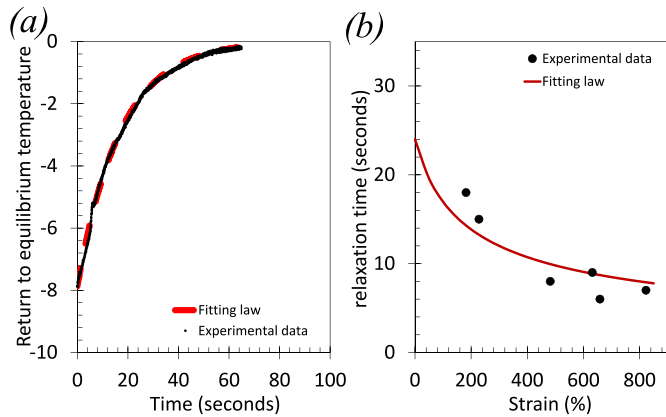


Fig. 9. (a) Example of return to equilibrium temperature measured on surface of the TPUU30 after unloading. The fitting law corresponds to Equation (5). From such equations the characteristic time of return to equilibrium temperature is calculated at different levels of deformation (cooling down to room temperature in the deformed state after loading or heating up to room temperature in the relaxed state after unloading). (b) Characteristic times versus strain for all four materials and for the two above-mentioned conditions (heating or cooling to room temperature. The fitting law corresponds to Equation (6) and the initial time (τ_0) has been calculated assuming a better fit for all four materials.

failure that includes: thermoelasticity, viscoelasticity, strain induced crystallization and damage mechanisms at the origin of macroscopic failure. In the following, cyclic tests are performed with relaxation phases of 60 s to allow a return to equilibrium temperature. This would

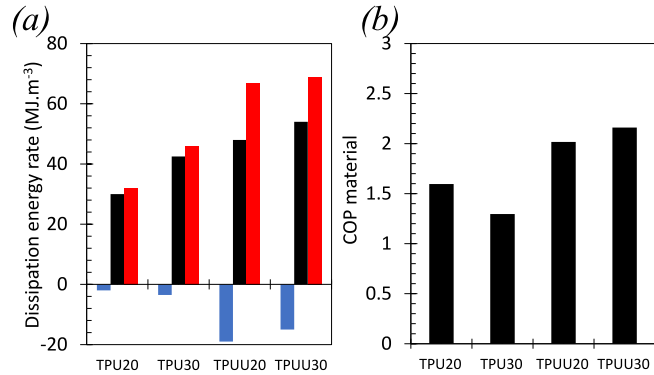


Fig. 11. (a) Dissipation energy rate, φ , calculated from Equation (9) (black filled column), dissipation energy rate during loading, φ_+ , (red filled columns, positive values), dissipation energy rate during unloading, φ_- , (red filled columns, negative values). We use the following relation: $\varphi = \varphi_+ + \varphi_-$. (b) Coefficient of performance of the materials, COP_{mat} , calculated as the ratio of dissipation energy rate, φ , calculated from Equation (9) and the dissipated mechanical energy calculated from Equation (8).

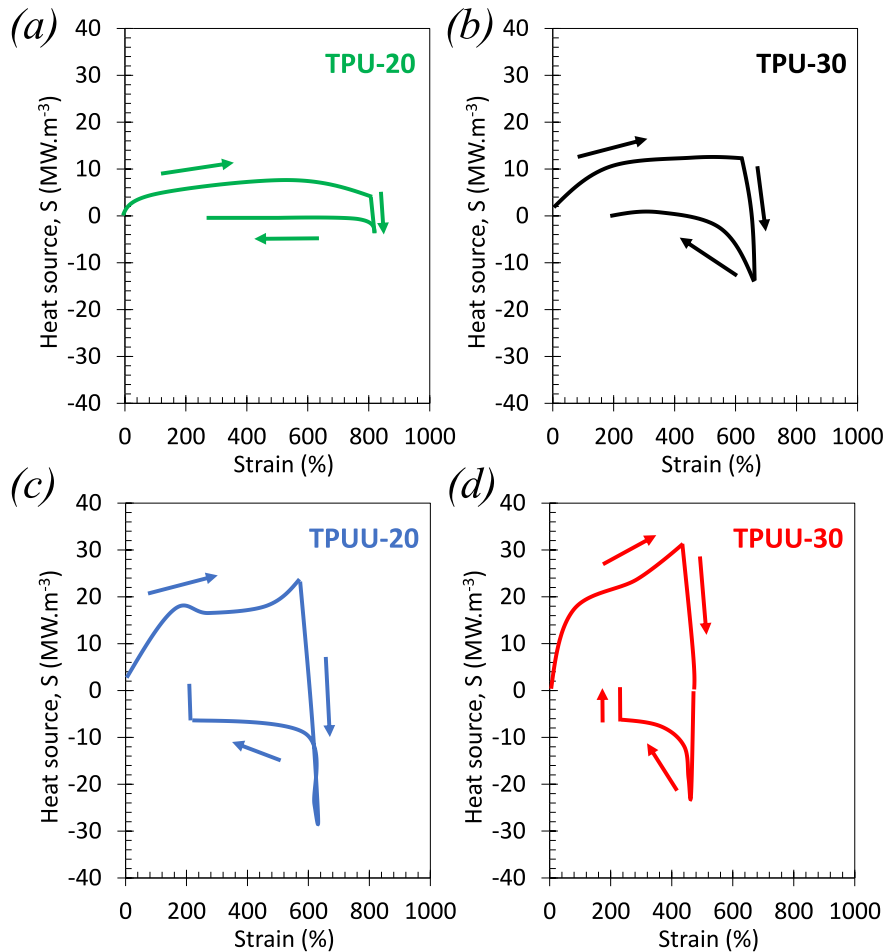


Fig. 10. Heat sources versus strain for TPU20 (a), TPU30 (b), TPUU20 (c) and TPUU30 (d) calculated from Equation (4). Arrows indicate the direction of the cycle.

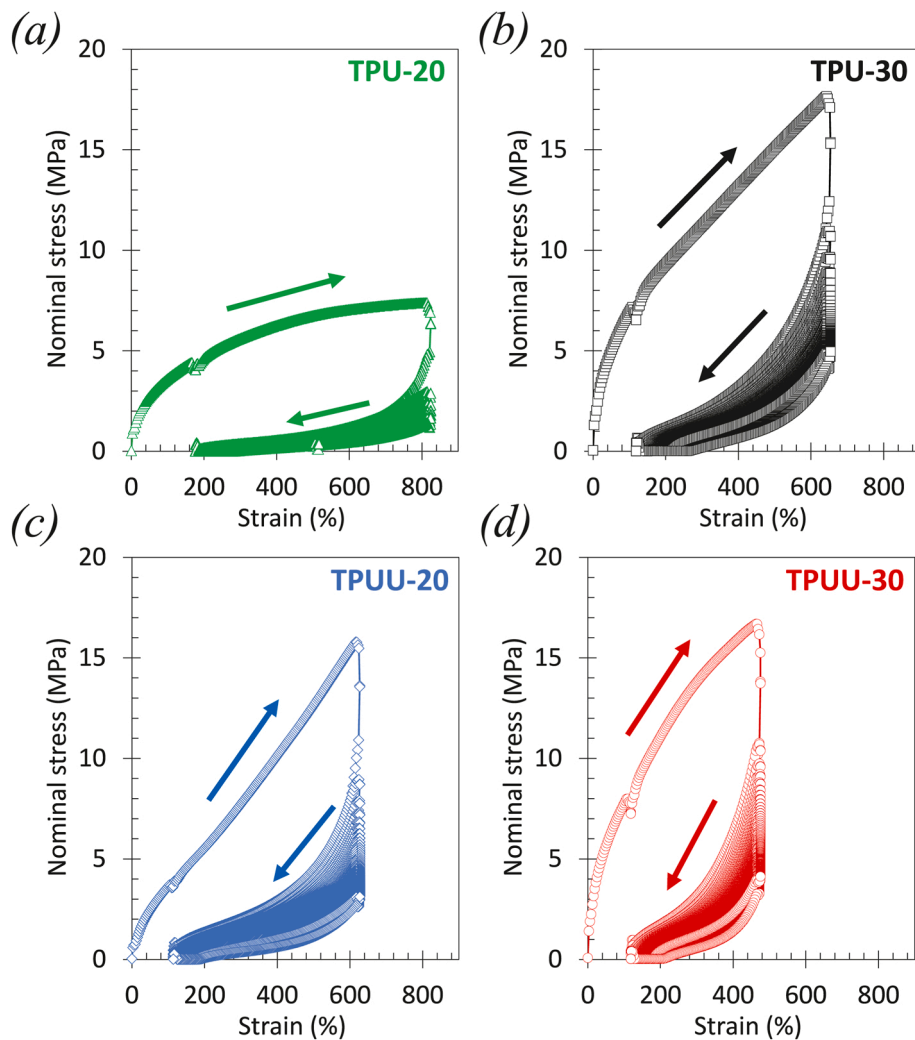


Fig. 12. Cyclic tests after pre-deformation. (a) Nominal stress of TPU20 (PEO-2K with 22 % HS), TPUU20 (PTMO-2K with 22 % HS), TPU30 (PEO-2K with 30 % HS) and TPUU30 (PTMO-2K with 30 % HS), (b) maximum stress during the cycles and (c) maximum temperature during the cycles. Arrows are indicated for the first cycle of the series.

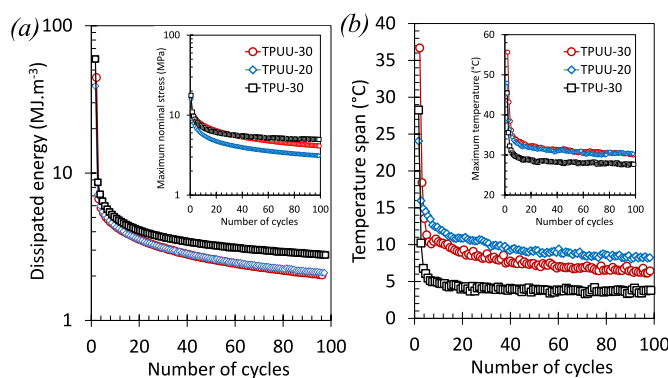


Fig. 13. Cyclic tests after pre-deformation. (a) Dissipated energy of TPU20 (PEO-2K with 22 % HS), TPUU20 (PTMO-2K with 22 % HS), TPU30 (PEO-2K with 30 % HS) and TPUU30 (PTMO-2K with 30 % HS), in insert the maximum nominal stress measured during the same series of cycles. (b) temperature span (difference between maximum temperature and minimum temperature of a cycle) during the same tests. In insert, the maximum temperature measured at the end of loading of each cycle.

allow us to discriminate different types of dissipative mechanisms. Some of these mechanisms are expected to show reversibility, such as the crystallization/melting or the thermoelasticity. Contrarily, viscoelastic effect and damage are irreversible dissipative mechanisms, within the time of the experiments.

Cyclic tests were performed up to maximum deformations before failure (Fig. 8a-b and Fig. S2). All curves show large hysteresis attesting for important mechanical dissipation, attributed to crystallization/melting, viscoelastic effects or damage of soft segment matrices or elastically active hard segments networks. Temperature change confirms the presence of irreversible mechanisms during cyclic tests as heating during loading is found significantly higher when compared to cooling during unloading. Nonetheless, it appears clearly that the cooling ability of the TPUUs is more important than that of the TPUs. This suggests higher contribution of reversible mechanisms such as thermoelasticity and latent heat associated with higher amorphous chains orientation and their subsequent strain induced crystallization, respectively. One may note that during such tests, possible re-crystallization or melting of thermally induced crystals will not be observed since their re-crystallization temperature is around 2–4 °C for TPU20 and TPUU20 or -43 °C for TPU30 are much below the lowest temperature experienced by all materials (during in-situ IR, the lowest temperature is found for the TPUU20 measured at 25°C–10 °C = 15 °C, see Fig. 8b). One may note that the highest heating is observed in PUs

with larger quantity of hard segments in both TPUs and TPUUs. This is likely due to the stiffer elastically active network of hard segments that promotes dissipative mechanisms. To discuss it, swelling experiments have been performed. Pus have been immersed into cyclohexane (50 mg of material into 30 mL of solvent for 24 h) have shown that TPUs do not swell, due to their polar nature (hydrophilic) and the mass ratio (mass of swollen material over mass of dry material) is found equal to 1.045 (± 0.05) and 1.041 (± 0.05) for TPU20 and TPU30 respectively. Contrarily, due to their less polar nature, TPUUs are more compatible with cyclohexane. Their mass ratio is found equal to 2.03 (± 0.05) and 1.64 (± 0.05) for TPUU20 and TPUU30 respectively. The lowest ratio in TPUU30 suggests a stiffer elastically active network of hard segment that promote dissipative mechanisms due to the multiple mechanisms previously discussed (entropic elasticity, viscoelasticity). However, the role of such elastically active network on the SIC ability is not so clear, as a too dense network may impede the growth of SIC crystals as has been discussed in the case of vulcanized naturel rubbers [48,49].

The treatment of heat sources presented in section 2.9 is used to reveal the contribution of reversible and irreversible deformation mechanisms implied in the caloric properties of the TPU and TPUUs studied. First of all, the time constant τ (s) characteristic of the heat exchange expressed in equations (5) and (6), is an important parameter to calculate the heat sources (equation (4)). It has been determined by fitting the curves of return to equilibrium temperature of the cyclic test shown in Fig. 9 (using the relaxation phases in both deformed and undeformed state). An example of return to cooled surface after unloading of the TPUU30 is shown in Fig. 9a. The resulting characteristic time is shown as a function of the strain for all materials and all conditions (right after loading and right after unloading). A general trend of decreased characteristic time with strain is observed, which is expected due to the reduction in materials thickness which eases heat transfer in the direction perpendicular to the samples surface. A simple law of strain dependence of this characteristic time (Equation (6)) is found to fit reasonably well with the experimental data as shown in Fig. 9b (it is assumed that such law is independent on the studied TPU and TPUU). It is worth noting that the time for return to equilibrium temperature is found to be much lower as compared to natural rubber with similar initial thickness [7] (characteristic time of 12 s at 500 % strain at compared to 26s in NR in similar experimental conditions and similar materials geometries), highlighting the interest of PUs as eC materials in real conditions, i.e., cyclic loadings where rapid heat exchanges are required.

The heat sources (Equation (4)) are calculated from the knowledge of the characteristic time for heat transfer to the specimen surface. We assume in this study that within the range of temperatures changes undergone by the materials, the c_p does not change substantially, and its value at room temperature is assumed to be a fixed parameter.

One may note first, like for the direct measure of the temperature changes (Fig. 8), that heat sources are found asymmetric between loading and unloading phases. The TPUU shows much higher heat source (during loading) and heat sink (during unloading) suggesting a higher overall elastocaloric effect. It is worth noting that the heat source increases immediately after the loading, for all materials, while at such deformation SIC did not occur yet (see Fig. 4). Such observation suggests the importance of thermoelastic effects due to entropic elasticity arising from amorphous chains orientation along a stretching axis that contribute dominantly to the elastocaloric behaviour at low strain (up to 200 % strain). One may note also that damage mechanisms should participate in dissipative mechanisms during loading, even at low deformation. In addition, the strong heat source changes when TPUU20 and TPUU30 are close to the ultimate unloading strain (sudden changes of 8 MW m^{-3} at 200 % of deformation) seems not correlated with the observation of a progressive return to isotropic state of the amorphous chains of soft segments during the unloading phase (cf. Fig. 5). At higher strain, heat source is found to almost stabilize for the TPU samples. Contrarily, an upturn of the heat sources is found in TPUUs at a strain

between 300 % and 400 %. It is not possible to correlate directly such behaviour with the occurrence of SIC that cumulates with thermoelasticity. Nonetheless, it appears clearly that the cooling capacity is higher in the case of the TPUUs. It is expected that the SIC crystals formed during the loading completely melt during unloading, generating the same heat source and heat sink related to such mechanism. Asymmetry in heat source/sink is due to other irreversible dissipative mechanisms (within the duration of the tensile test) such as viscoelasticity or damage. Further treatment of the heat sources is proposed in the following to more properly quantify the reversible and irreversible dissipative mechanisms.

The comparison of mechanical energy dissipation between all materials as well as possible role of crystallization/melting in the eC of the PUs is not trivial as all polyurethanes have not been extended up to the same deformation. To tackle this, a treatment of heat sources is used, and mean dissipation energy rate is calculated using Equation (9). The ratio of this rate over mechanical energy over the cycles provides information on coefficient of performance (COP) of the materials (cf. Equation (10)). A separation of dissipation energy rate during loading, named ϕ_+ and dissipation energy rate during unloading, named ϕ_- . ϕ_+ contains, while not exclusively, the information of the crystallinity (crystal volume fraction induced by deformation). From the integration over time of the heat sources, and as an expected result from the observed asymmetry, the dissipation energy rate over the cycle, ϕ , is found to be positive for all materials, with the highest values for the TPUUs (Fig. 11a). The dissipation energy rate during loading, ϕ_+ , is also found to be the highest for the TPUUs. It is worth noting that the dissipation energy rate during unloading, ϕ_- is found to be negligible for the TPUs (ϕ_- is only 6 and 7 % of the value of ϕ_+ for TPU20 and TPU30 respectively) and significant for the TPUUs (ϕ_- is 28 and 22 % of the value of ϕ_+ for TPUU20 and TPUU30 respectively). While a direct correlation with in-situ WAXS cannot be established, due to different experimental conditions with in-situ IR tests (different nominal strain rates, different maximum strain), such results indicate a higher reversibility of heat sources in TPUUs, likely caused by a higher contribution of thermoelasticity arising from higher amorphous chains orientation and higher latent heat of phase changes due to SIC and melting. As a consequence, the COP_{mat} of the TPUUs is found to be higher than those of the TPUs (Fig. 11b). Nonetheless, COP_{mat} values are found to be quite low as compared to other elastomeric caloric materials, such as natural rubber, which can reach a value of 4, under similar experiment conditions [7]. This is likely attributed to the high mechanical dissipation that happens during a single cycle in PUs, caused by high viscoelasticity and damage mechanisms, especially from irreversible breakage of strongly hydrogen bonded hard segment network, and eventually disentanglement and breakage of soft segment, similar to what may happen in unfilled rubber-based materials showing close mechanical properties [50,51]. Higher COP_{mat} values can be obtained by limiting damage and limiting viscoelasticity. This can be achieved by performing series of mechanical cycles and allow the materials to accommodate the deformation with cyclic loadings.

For the cyclic tests, specimens have been cycled 100 times up to the same maximum strain value as for the single loading tests (Fig. 11). Results show a clear stress accommodation from first to following cycles for all four materials (Fig. 12). Moreover, the mechanical hysteresis is found to drastically decrease with the accumulation of cycles, especially between the first and following cycles. Dissipated mechanical energy (Fig. 13a) and temperature span (Fig. 13b) are calculated from the area of mechanical cycles and from the maximum temperature changes in the cycles, respectively. Dissipated mechanical energy is dramatically reduced with the cycle accumulation, with the main accommodation occurring between first and second cycle (same trend applies to the maximum stress measured at each cycle, see insert of Fig. 13a). Such mechanical energy accommodation suggests a reduction of dissipation mechanisms between the first and following cycles, that may arise from a completion of most of damage, H-bonding breakage in hard segments

or chains scission in the soft phase during the first cycle. One may note that the TPU20 has not been studied at this stage due to the absence of cooling abilities (see Figs. 8b and 10a) that is related primarily to its absence of strain induced crystallization (Fig. 4) and low amorphous chains orientation (Fig. 5), limiting its elastocaloric behaviour.

From the determination of both dissipative thermal and mechanical energy, the materials COP, COP_{mat} , can be calculated (see calculation previously made for the single cyclic tests). Fig. 14 shows the changes in COP_{mat} for TPU-30, TPUU-20 and TPUU-30. COP_{mat} is found to drastically increase with cycle accumulation. This is primarily attributed to transition from first to second cycle. Most of the COP_{mat} is found to increase from the first to second cycle (relative increase of 250 %, 360 % and 320 % for TPU-20, TPUU-20 and TPUU-30 respectively), but it is worth noticing that from second to 100th cycle, non-negligible increase is observed, especially for the TPUU-30 (relative increase of 30 %, 30 % and 270 % for TPU-20, TPUU-20 and TPUU-30 respectively), confirming a great eC property in such material. Not only the COP_{mat} is of great importance when targeting industrial cooling but also the temperature span (The temperature span is the maximum temperature difference established between the heat sink and the heat source in a cooling system) (see Fig. 15).

It is common to represent the COP_{mat} versus the temperature span to underline the capability of such cooling systems. Consistent with previous discussion, COP_{mat} is found to increase for all three PUs systems, while temperature span decreases (Fig. 13b). Such values are compared with values obtained by Coativi et al. [52] that is, from the best of our knowledge, the first investigation of the eC effect in purely elastomeric polyurethanes. In similar conditions (pre-deformation and cyclic loading up to 100 cycles), they found a relationship between COP_{mat} and ΔT (couple of values 3.5–8 for ΔT - COP_{mat}) similar to what we found in the TPUU30. One may note that, tuning the content in HS segment (from 30 to 20 wt%), such relationship can be substantially increased up to a couple of values of 8.8–12.6 for ΔT - COP_{mat} in TPUU20. As was discussed previously, the hard segments, as anchoring point for the soft

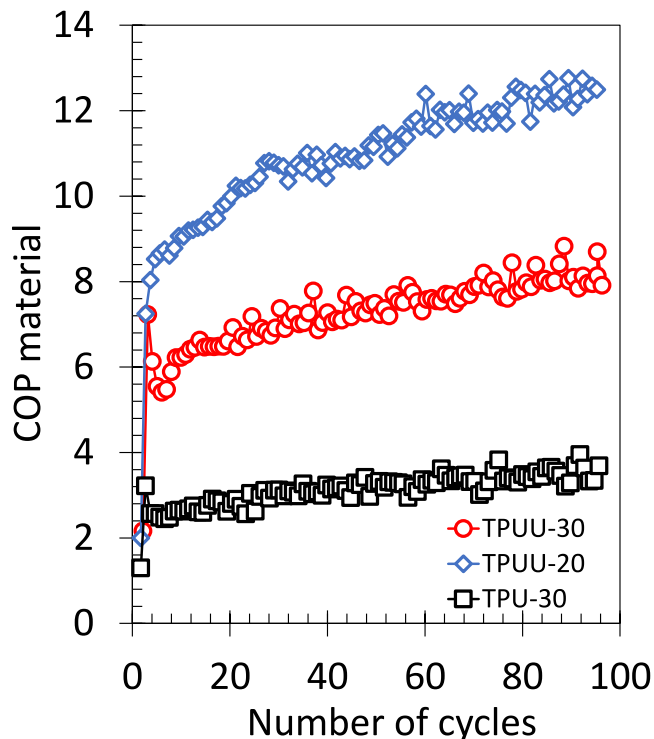


Fig. 14. Materials coefficient of performance (COP_{mat}) of TPU-30, TPUU-20 and TPUU-30 during 100 cycles.

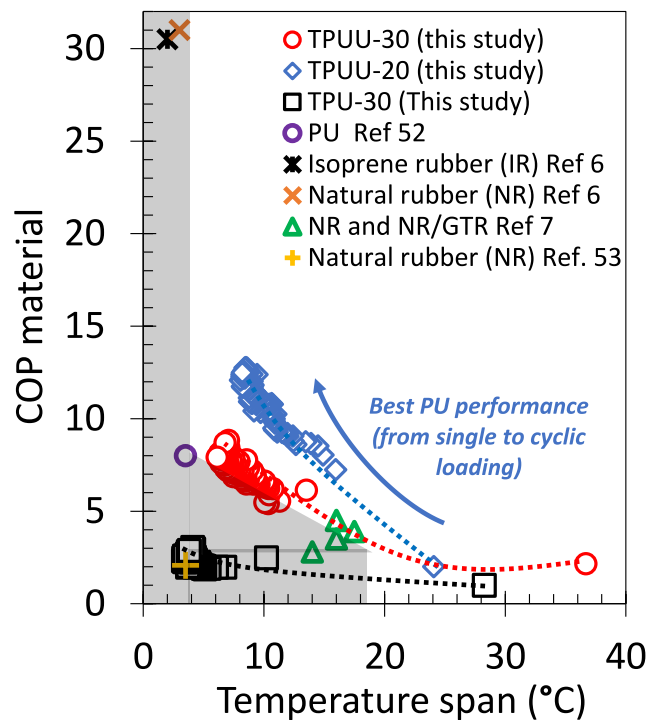


Fig. 15. Materials coefficient of performance (COP_{mat}) of TPU-30, TPUU-20 and TPUU-30 changes during the application of 100 cycles versus temperature span. Comparison with other elastocaloric and elastomeric materials from the literature. The grey area covers the elastomer literature. Dotted lines indicate the evolution of the COP_{mat} of our materials as a function of the cycles (from low to high number of cycles, the COP_{mat} increases while the temperature span decreases).

segments chains orientation and subsequent strain induced crystallization, is determinant in the eC effect. But a too high content may hinder the proper development (eventually the growth) of SIC crystals. Such statement should however be confirmed by more precise analysis of the SIC microstructure in PUs systems for series of PUs with diverse HS contents. The comparison with other elastocaloric elastomeric materials is also crucial. Natural rubber (NR) and their synthetic equivalents (polyisoprene rubber, IR) are known to undergo large eC effect IR [6, 7, 53]. Depending on the mechanical solicitation (single or continuous loading), the balance between COP_{mat} and ΔT is widely modified. In single loading tests, COP_{mat} is low (around 4–5) but the ΔT is high (around 10–20 °C) [7]. During dynamic cycles, the COP_{mat} is high (around 30) due to high stress accommodation and very low mechanical hysteresis, but the dynamic strain range is not high enough to significantly generate thermal exchanges (through both entropic elasticity and SIC). Finally, if one aims to compare with non-elastomeric materials, PUs compete well with conventional elastocaloric shape memory alloys, such as Ni–Ti systems [54].

4. Conclusion

This work provides direct microstructural evidence that both amorphous chain orientation and strain-induced crystallization (SIC) contribute to the elastocaloric (eC) effect in thermoplastic polyurethanes (TPUs). Using a combination of in situ WAXS and infrared thermography, we demonstrated that the orientation of amorphous chains occurs early in the deformation process for all TPU systems. In PTMO based TPUUs which show strain induced crystallization this orientation facilitates SIC, which begins around 100 % strain and contributes substantially to the eC response via the latent heat of

crystallization and melting. In contrast, PEO based TPUs which do not display strain induced crystallization, show limited orientation and negligible SIC, leading to weaker and less reversible eC effects.

Cyclic loading experiments further revealed that TPUs exhibit greater reversibility in temperature change, supporting a more prominent role of reversible mechanisms like thermoelasticity and SIC. TPUs showed higher elastocaloric heating and cooling, higher dissipation energy during unloading, and notably better coefficients of performance (COP) compared to TPU. Additionally, stress relaxation and reduced mechanical hysteresis after initial cycles point to a stabilizing of the microstructure, enhancing eC efficiency.

Our results suggest that optimizing the balance between amorphous orientation and crystallization—via tailored segment composition and morphology—can significantly boost eC performance. This work highlights the importance of integrating structural analysis with thermal response metrics to decipher and engineer the mechanisms behind the elastocaloric effect in polymers. It provides a roadmap for designing next-generation elastocaloric materials that combine high cooling efficiency with mechanical durability for scalable, flexible, and environmentally friendly cooling technologies.

CRediT authorship contribution statement

Nicolas Candau: Writing – review & editing, Writing – original draft, Visualization, Validation, Supervision, Methodology, Investigation, Funding acquisition, Formal analysis, Data curation, Conceptualization. **Oguzhan Oguz:** Writing – review & editing, Supervision, Methodology, Investigation, Data curation, Conceptualization. **Gizem Kurtulmus:** Methodology, Investigation, Formal analysis, Data curation. **Emel Yilgor:** Supervision, Investigation. **Yusuf Z. Menceloglu:** Supervision, Methodology, Investigation, Formal analysis, Data curation. **Iskender Yilgor:** Supervision, Methodology, Investigation, Formal analysis, Conceptualization.

Declaration of competing interest

The authors declare that they have no known competing financial interests or personal relationships that could have appeared to influence the work reported in this paper.

Acknowledgements

The authors acknowledge the group eb-POLICOM: Polímers i Composites Ecologics i Biodegradables, a research group of the Generalitat de Catalunya (Grant 2021 SGR 01042). This work is part of María de Maeztu Units of Excellence Programme CEX2023-001300-M/funded by MICIU/AEI/10.13039/501100011033. These experiments were performed at BL11-NCD-SWEET beamline at ALBA Synchrotron with the collaboration of ALBA staff, Marc Malfois and Cristian Huck Iriart.

Appendix A. Supplementary data

Supplementary data to this article can be found online at <https://doi.org/10.1016/j.polymer.2025.129225>.

Data availability

Data will be made available on request.

References

- [1] A review and analysis of the elasto-caloric effect for solid-state refrigeration devices: challenges and opportunities, *MRS Energy Sustain.* 2 (2015) E16.
- [2] M. Imran, X. Zhang, Recent developments on the cyclic stability in elastocaloric materials, *Mater. Des.* 195 (Oct. 2020) 109030, <https://doi.org/10.1016/j.matdes.2020.109030>.
- [3] S. Qian, et al., A review of elastocaloric cooling: materials, cycles and system integrations, *Int. J. Refrig.* 64 (Apr. 2016) 1–19, <https://doi.org/10.1016/j.ijrefrig.2015.12.001>.
- [4] Y. Yoshida, K. Yuse, D. Guyomar, J.-F. Capsal, G. Sebald, Elastocaloric effect in poly(vinylidene fluoride-trifluoroethylene-chlorotrifluoroethylene) terpolymer, *Appl. Phys. Lett.* 108 (24) (Jun. 2016) 242904, <https://doi.org/10.1063/1.4953770>.
- [5] S. Zhang, et al., Solid-state cooling by elastocaloric polymer with uniform chain-lengths, *Nat. Commun.* 13 (1) (Jan. 2022) 9, <https://doi.org/10.1038/s41467-021-27746-y>.
- [6] H. Haissoune, G. Coativy, L. Chazeau, L. Lebrun, G. Sebald, J.-M. Chenal, Critical parameters governing elastocaloric effect in polyisoprene rubbers for solid-state cooling, *Polymer* 307 (Jul. 2024) 127234, <https://doi.org/10.1016/j.polymer.2024.127234>.
- [7] N. Candau, E. Vives, A.I. Fernández, M.L. Maspoch, Elastocaloric effect in vulcanized natural rubber and natural/wastes rubber blends, *Polymer* 236 (Nov. 2021) 124309, <https://doi.org/10.1016/j.polymer.2021.124309>.
- [8] N. Candau, A. Zimny, E. Vives, M.L. Maspoch, Elastocaloric waste/natural rubber materials with various crosslink densities, *Polymers* 15 (11) (Jan. 2023), <https://doi.org/10.3390/polym15112566>, , Art. no. 11.
- [9] J. Tušek, K. Engelbrecht, D. Eriksen, S. Dall’Olio, J. Tušek, N. Pryds, A regenerative elastocaloric heat pump, *Nat. Energy* 1 (10) (Sep. 2016) 1–6, <https://doi.org/10.1038/nenergy.2016.134>.
- [10] Z. Xie, G. Sebald, D. Guyomar, Comparison of elastocaloric effect of natural rubber with other caloric effects on different-scale cooling application cases, *Appl. Therm. Eng.* 111 (Jan. 2017) 914–926, <https://doi.org/10.1016/j.applthermaleng.2016.09.164>.
- [11] F.C. Colman, et al., On the mechanocaloric effect of natural graphite/thermoplastic polyurethane composites, *J. Mater. Sci.* 58 (27) (Jul. 2023) 11029–11043, <https://doi.org/10.1007/s10853-023-08700-3>.
- [12] K. Wang, J.T.B. Overvelde, K. Engelbrecht, R. Bjørk, C.R.H. Bahl, Volume compensation of large-deformation 3D-printed soft elastomeric elastocaloric regenerators, *Appl. Phys. Lett.* 123 (22) (Nov. 2023) 223904, <https://doi.org/10.1063/5.0177761>.
- [13] K. Wang, K. Engelbrecht, C.R.H. Bahl, Additive manufactured thermoplastic elastomers for low-stress driven elastocaloric cooling, *Appl. Mater. Today* 30 (Feb. 2023) 101711, <https://doi.org/10.1016/j.apmt.2022.101711>.
- [14] H. Xiong, et al., Healable and recyclable polyurethane with natural-rubber-like resilience via π -Type tweezer structure stabilizing dynamical hard domains, *Macromolecules* 56 (21) (Nov. 2023) 8581–8591, <https://doi.org/10.1021/acs.macromol.3c01770>.
- [15] C. Zhang, et al., Renewable castor-oil-based waterborne polyurethane networks: simultaneously showing high strength, self-healing, processability and tunable multishape memory, *Angew. Chem. Int. Ed.* 60 (8) (2021) 4289–4299, <https://doi.org/10.1002/anie.202014299>.
- [16] J. Hao, et al., A device-quality thermosetting polyurethane with improved processability and high thermal stability of dipole alignment for electro-optic applications, *React. Funct. Polym.* 66 (8) (Aug. 2006) 832–839, <https://doi.org/10.1016/j.reactfunctpolym.2005.11.016>.
- [17] S. Damrongasakkul, R. Sinweeruthai, J.S. Higgins, Processability and chemical resistance of the polymer blend of thermoplastic polyurethane and polydimethylsiloxane, *Macromol. Symp.* 198 (1) (2003) 411–420, <https://doi.org/10.1002/masy.200350835>.
- [18] J. Xu, et al., Recent advances in high-strength and high-toughness polyurethanes based on supramolecular interactions, *Polym. Chem.* 13 (17) (May 2022) 2420–2441, <https://doi.org/10.1039/D2PY00269H>.
- [19] Q. Qu, et al., High toughness polyurethane toward artificial muscles, tuned by mixing dynamic hard domains, *Macromolecules* 54 (17) (Sep. 2021) 8243–8254, <https://doi.org/10.1021/acs.macromol.1c01098>.
- [20] H. Li, et al., High modulus, strength, and toughness polyurethane elastomer based on unmodified lignin, *ACS Sustain. Chem. Eng.* 5 (9) (Sep. 2017) 7942–7949, <https://doi.org/10.1021/acssuschemeng.7b01481>.
- [21] N. Candau, et al., Stiff, strong, tough, and highly stretchable hydrogels based on dual stimuli-responsive semicrystalline Poly(urethane–urea) copolymers, *ACS Appl. Polym. Mater.* 3 (11) (Nov. 2021) 5683–5695, <https://doi.org/10.1021/acsapm.1c00969>.
- [22] O. Oguz, et al., Geometric confinement controls stiffness, strength, extensibility, and toughness in poly(urethane–urea) copolymers, *Macromolecules* 54 (10) (May 2021) 4704–4725, <https://doi.org/10.1021/acs.macromol.1c00596>.
- [23] M. Choi, et al., Functionalized polyurethane-coated fabric with high breathability, durability, reusability, and protection ability, *Adv. Funct. Mater.* 31 (24) (2021) 2101511, <https://doi.org/10.1002/adfm.202101511>.
- [24] M. Küttig, Jan Roggenkamp, Ute Urban, Schmitz-Rode, Thomas, U, Steinseifer, Polyurethane heart valves: past, present and future, *Expt Rev. Med. Dev.* 8 (2) (Mar. 2011) 227–233, <https://doi.org/10.1586/erd.10.79>.
- [25] H. Zhang, L. An, X. Wang, C. Niu, X. Hou, A colorless, transparent and mechanically robust polyurethane elastomer: synthesis, chemical resistance and adhesive properties, *New J. Chem.* 46 (10) (Mar. 2022) 4762–4771, <https://doi.org/10.1039/D1NJ05874F>.
- [26] A. Hansen, M. Renner, A.G. Griesbeck, T. Büsgen, From 3D to 4D printing: a reactor for photochemical experiments using hybrid polyurethane acrylates for vat-based polymerization and surface functionalization, *Chem. Commun.* 56 (96) (Dec. 2020) 15161–15164, <https://doi.org/10.1039/D0CC06512A>.
- [27] M.Y.L. Chew, Resistance of polyurethane sealants to hot water, *Build. Res. Inf.* 30 (5) (Sep. 2002) 367–371, <https://doi.org/10.1080/09613210210143340>.

- [28] J. Zhang, et al., Unveiling the hierarchical microstructure of prevulcanized natural rubber latex film and its impact on mechanical properties, *Macromolecules* 57 (24) (Dec. 2024) 11727–11737, <https://doi.org/10.1021/acs.macromol.4c02599>.
- [29] Q. Teng, Y. Huang, H. Wu, W. Li, Q. Wu, J. Wu, Self-healing polyurethane elastomer with ultra-high mechanical strength and enhanced thermal mechanical properties, *Polymer* 290 (Jan. 2024) 126579, <https://doi.org/10.1016/j.polymer.2023.126579>.
- [30] S. Das, et al., Effect of symmetry and h-bond strength of hard segments on the structure-property relationships of segmented, nonchain extended polyurethanes and polyureas, *J. Macromol. Sci. Part B* 46 (5) (Aug. 2007) 853–875, <https://doi.org/10.1080/00222340701388805>.
- [31] A. Kuta, Zdeněk Hrdlička, Adam Strachota, M. Špírková, The influence of macrodiol type on the mechanical properties of polyurethane materials, *Mater. Manuf. Process.* 24 (10–11) (Oct. 2009) 1214–1216, <https://doi.org/10.1080/10426910902979553>.
- [32] D.B. Klinedinst, I. Yilgör, E. Yilgör, M. Zhang, G.L. Wilkes, The effect of varying soft and hard segment length on the structure–property relationships of segmented polyurethanes based on a linear symmetric diisocyanate, 1,4-butanediol and PTMO soft segments, *Polymer* 53 (23) (Oct. 2012) 5358–5366, <https://doi.org/10.1016/j.polymer.2012.08.005>.
- [33] P. Zhu, X. Dong, D. Wang, Strain-Induced crystallization of segmented copolymers: deviation from the classic deformation mechanism, *Macromolecules* 50 (10) (May 2017) 3911–3921, <https://doi.org/10.1021/acs.macromol.6b02747>.
- [34] N. Tian, et al., Extension flow induced crystallization of poly(ethylene oxide), *Macromolecules* 44 (19) (Oct. 2011) 7704–7712, <https://doi.org/10.1021/ma201263z>.
- [35] B. Zhao, et al., Inducing crystallization of polymer through stretched network, *Macromolecules* 42 (5) (Mar. 2009) 1428–1432, <https://doi.org/10.1021/ma802679h>.
- [36] N. Tian, et al., Confined crystallization in end-linked PEO network under uniaxial extension, *Polymer* 54 (26) (Dec. 2013) 7088–7093, <https://doi.org/10.1016/j.polymer.2013.10.055>.
- [37] N. Candau, et al., Mechanical reinforcement and memory effect of strain-induced soft segment crystals in thermoplastic polyurethane-urea elastomers, *Polymer* 223 (May 2021) 123708, <https://doi.org/10.1016/j.polymer.2021.123708>.
- [38] J. Zhang, Y. Wu, Y. Lv, G. Zhu, Y. Zhu, Mechanocaloric effects characterization of low-crystalline thermoplastic polyurethanes fiber, *Polymers* 16 (23) (Nov. 2024), <https://doi.org/10.3390/polym16233360>, 3360.
- [39] G.R. Mitchell, A.H. Windle, The determination of molecular orientation in uniaxially compressed PMMA by X-ray scattering, *Polymer* 24 (3) (Mar. 1983) 285–290, [https://doi.org/10.1016/0032-3861\(83\)90264-1](https://doi.org/10.1016/0032-3861(83)90264-1).
- [40] 'Mechanical Properties of Solid Polymers - Ian M. Ward, John Sweeney - Google Livres' Accessed: Apr. 01, 2025. [Online]. Available: https://books.google.es/books?hl=fr&lr=&id=oafPBe3QarkC&oi=fnd&pg=PR13&dq=I.+M.+Ward,+and+J.+Sweeney,+Mechanical+Properties+of+Solid+Polymers,+John+Wiley+%26+Sons,+2012.&ots=I9JgUlk20&sig=Y00xGx9QpcwaVg5FVwCo_rdvI#v=onepage&q=I.%20M.%20Ward%2C%20and%20J.%20Sweeney%2C%20Mechanical%20Properties%20of%20Solid%20Polymers%2C%20John%20Wiley%20%26%20Sons%2C%202012.&f=false
- [41] A. Benaarbia, A. Chrysochoos, G. Robert, Kinetics of stored and dissipated energies associated with cyclic loadings of dry polyamide 6.6 specimens, *Polym. Test.* 34 (Apr. 2014) 155–167, <https://doi.org/10.1016/j.polymertesting.2014.01.009>.
- [42] J.R. Samaca Martinez, J.-B. Le Cam, X. Balandraud, E. Toussaint, J. Caillard, Filler effects on the thermomechanical response of stretched rubbers, *Polym. Test.* 32 (5) (Aug. 2013) 835–841, <https://doi.org/10.1016/j.polymertesting.2013.04.003>.
- [43] P. Zhu, et al., Reversible–Irreversible transition of strain-induced crystallization in segmented copolymers: the critical strain and chain conformation, *ACS Appl. Polym. Mater.* 3 (7) (Jul. 2021) 3576–3585, <https://doi.org/10.1021/acsapm.1c00462>.
- [44] F. Yeh, B.S. Hsiao, B.B. Sauer, S. Michel, H.W. Siesler, In-Situ studies of structure development during deformation of a segmented Poly(urethane–urea) elastomer, *Macromolecules* 36 (6) (Mar. 2003) 1940–1954, <https://doi.org/10.1021/ma0214456>.
- [45] J. Rault, J. Marchal, P. Judeinstein, P.A. Albouy, Stress-induced crystallization and reinforcement in filled natural rubbers: 2H NMR study, *Macromolecules* 39 (24) (Nov. 2006) 8356–8368, <https://doi.org/10.1021/ma0608424>.
- [46] E. Unsal, B. Yalcin, I. Yilgor, E. Yilgor, M. Cakmak, Real time mechano-optical study on deformation behavior of PTMO/CHDI-based polyetherurethanes under uniaxial extension, *Polymer* 50 (19) (Sep. 2009) 4644–4655, <https://doi.org/10.1016/j.polymer.2009.07.041>.
- [47] I.I. Nugay, C. Kosak, E. Unsal, E. Yilgor, M. Cakmak, Fast-tracking of the segmental orientation in Poly(ethylene oxide)-based polyurethane urea by mechano-optical (infrared dichroism and birefringence) properties: degree of the soft-segment ordering effect, *Macromolecules* 56 (2) (Jan. 2023) 601–611, <https://doi.org/10.1021/acs.macromol.2c01473>.
- [48] J.-M. Chenal, L. Chazeau, L. Guy, Y. Bomal, C. Gauthier, 'Molecular weight between physical entanglements in natural rubber: a critical parameter during strain-induced crystallization', *Polymer* 48 (4) (Feb. 2007) 1042–1046, <https://doi.org/10.1016/j.polymer.2006.12.031>.
- [49] N. Candau, L. Chazeau, J.-M. Chenal, C. Gauthier, E. Munch, Complex dependence on the elastically active chains density of the strain induced crystallization of vulcanized natural rubbers, from low to high strain rate, *Polymer* 97 (Aug. 2016) 158–166, <https://doi.org/10.1016/j.polymer.2016.05.020>.
- [50] N. Candau, O. Oguz, E. Peuvrel-Disdier, J.-L. Bouvard, C. Pradille, N. Billon, Strain-induced network chains damage in carbon black filled EPDM, *Polymer* 175 (Jun. 2019) 329–338, <https://doi.org/10.1016/j.polymer.2019.05.017>.
- [51] N. Candau, O. Oguz, E. Peuvrel-Disdier, J.-L. Bouvard, C. Pradille, N. Billon, Strain and filler ratio transitions from chains network to filler network damage in EPDM during single and cyclic loadings, *Polymer* 197 (May 2020) 122435, <https://doi.org/10.1016/j.polymer.2020.122435>.
- [52] G. Coatify, et al., Elastocaloric properties of thermoplastic polyurethane, *Appl. Phys. Lett.* 117 (19) (Nov. 2020) 193903, <https://doi.org/10.1063/5.0023520>.
- [53] R. Bennacer, B. Liu, M. Yang, A. Chen, Refrigeration performance and the elastocaloric effect in natural and synthetic rubbers, *Appl. Therm. Eng.* 204 (Mar. 2022) 117938, <https://doi.org/10.1016/j.applthermaleng.2021.117938>.
- [54] J. Chen, L. Lei, G. Fang, Elastocaloric cooling of shape memory alloys: a review, *Mater. Today Commun.* 28 (Sep. 2021) 102706, <https://doi.org/10.1016/j.mtcomm.2021.102706>.